Biosensors and Bioelectronics 79 (2016) 553–560

Contents lists available at ScienceDirect

Biosensors and Bioelectronics

journal homepage: www.elsevier.com/locate/bios

Protein-templated cobaltous phosphate nanocomposites for the highly sensitive and selective detection of platelet-derived growth factor-BB

Linghao He [a], Shuai Zhang [a], Hongfei Ji [a], Minghua Wang [b], Donglai Peng [a], Fufeng Yan [a], Shaoming Fang [a,b], Hongzhong Zhang [b], Chunxiao Jia [a,c], Zhihong Zhang [a,b,*]

[a] State Laboratory of Surface and Interface Science of Henan Province, Zhengzhou University of Light Industry, No. 166, Science Avenue, Zhengzhou 450001, PR China

[b] Henan Collaborative Innovation Center of Environmental Pollution Control and Ecological Restoration,Zhengzhou University of Light Industry, No. 166, Science Avenue, Zhengzhou 450001, PR China

[c] Henan Collaborative Innovation Center of Food Production and Safety, Zhengzhou University of Light Industry, No. 166, Science Avenue, Zhengzhou 450001, PR China

ARTICLE INFO

Article history:
Received 23 October 2015
Received in revised form
25 December 2015
Accepted 26 December 2015
Available online 29 December 2015

Keywords:
Cobaltous phosphate nanocomposites
Platelet-derived growth factor-BB
Aptasensor

ABSTRACT

We synthesized novel $Co_3(PO_4)_2$-based nanocomposites with 3D porous architectures via self-assembly; here, bovine serum albumin (BSA) and aptamer were used as organic phases to produce $Co_3(PO_4)_2$@BSA and $Co_3(PO_4)_2$@Apt nanocomposites, respectively. The formation mechanism of $Co_3(PO_4)_2$-based nanocomposites was described based on characterizations of their physio-chemical performance, and the developed nanocomposites were applied as scaffold materials to construct a novel electrochemical aptasensor and detect platelet-derived growth factor-BB (PDGF-BB). The PDGF-BB targeting aptamer must be immobilized onto the $Co_3(PO_4)_2$@BSA-modified electrode to detect PDGF-BB, whereas $Co_3(PO_4)_2$@Apt-based aptasensor may be directly used to determine the target protein. Electrochemical impedance spectroscopy results showed that the developed $Co_3(PO_4)_2$@BSA- and $Co_3(PO_4)_2$@Apt-based aptasensors present highly sensitive detection ability toward PDGF-BB. Due to the special nanoflower structure, the $Co_3(PO_4)_2$@BSA-based aptasensor features a detection limit of 3.7 pg mL^{-1}; while the limit of detection of the $Co_3(PO_4)_2$@Apt-based aptasensor is 61.5 pg mL^{-1}, which is the possible bioactivity loss of the aptamer in $Co_3(PO_4)_2$@Apt nanocomposite. The two detection limits obtained are still much lower than or comparable with those of previously reported aptasensors. The $Co_3(PO_4)_2$@BSA- and $Co_3(PO_4)_2$@Apt-based aptasensors showed high selectivity, stability, and applicability for detecting the desired protein. This finding indicates that the $Co_3(PO_4)_2$-based nanocomposites could be used as an electrochemical biosensor for various detection procedures in the biomedical field.

1. Introduction

Platelet-derived growth factor BB (PDGF-BB), a protein marker, is directly involved in many cell transformation processes, such as tumor growth and progression (Buchdunger et al., 2000; Fleming et al., 1992). As a widely used biomarker for hepatic fibrosis (Chen et al., 2008), liver cancer (Lau et al., 2009), and gastrointestinal stromal tumors (Janeway et al., 2007), PDGF has been implicated in the pathogenesis of angiogenesis in these tumor types. Thus, a rapid, sensitive, and accurate biomarker detection platform for PDGF quantification is of considerable importance for clinical diagnosis and related biomedical research. Several aptasensors have been developed for detecting PDGF-BB based on electrochemistry (Wang et al., 2009; Zuo et al., 2007), fluorescence (Ishii et al., 2011; Zayats et al., 2006), colorimetry (Chang et al., 2013), chemiluminescence (Wang et al., 2013), and electrochemiluminescence (Zhu et al., 2010). Among the existing aptasensors, electrochemical aptasensors based on the specificity of aptamer-target recognition have received particular attention because of their high sensitivity, low sample volume, short detection time, simple pretreatment procedure, inexpensive instrumentation, and automated detection (Hianik and Wang, 2009; Zelada-Guillén et al., 2010; Zhu et al., 2014). Different nanomaterials, including gold nanoparticles (Du et al., 2009), carbon nanostructures (Das et al., 2011; Liu et al., 2010), and quantum dots (Yuan et al., 2012), have been used to modify detection signals to obtain highly sensitive electrochemical aptasensors. However, many disadvantages, such as complicated procedures, high costs, and poor reproducibility and quantification, especially when complex samples are detected, have also

* Corresponding author at: State Laboratory of Surface and Interface Science of Henan Province, Zhengzhou University of Light Industry, No. 166, Science Avenue, Zhengzhou 450001, PR China.
E-mail address: mainzhh@163.com (Z. Zhang).

http://dx.doi.org/10.1016/j.bios.2015.12.095
0956-5663/

been observed in the application of these nanomaterials (Cheng et al., 2012; He et al., 2011). Thus, simple aptasensors for ultrasensitive and convenient detection of proteins remain an urgent need.

Moreover, biomolecules can provide chelating groups for the interaction with metal ions and act as capping agents for passivizing the surface of particles with a specific morphology or size; this approach to generate nanomaterials is somewhat similar to the biomineralization behavior of many organisms in nature. Ge et al. (2012) recently fabricated $Cu_3(PO_4)_3$ nanoflowers via self-assembly using BSA as a template (Ge et al., 2012). Afterwards, a series of organic–inorganic hybrids of $Cu_3(PO_4)_2$ was obtained by using enzymes as a template in phosphate buffer and applied to the sensing field (Huang et al., 2015; Lin et al., 2014; Sun et al., 2014). Zhang et al. (2015) discovered two kinds of $Mn_3(PO_4)_2$ nanoflowers using an antibody as a template and applied them to ractopamine detection (Zhang et al., 2015b). To date, few reports on nucleic acid-templated $Co_3(PO_4)_2$ are available. López-Gallego and Yate (2015) developed a novel bio-inorganic catalyst based on $Co_3(PO_4)_2$; they employed this catalyst for several redox reaction cycles (López-Gallego and Yate, 2015).

Amorphous $Co_3(PO_4)_2$ and a $Co_3(PO_4)_2$-ZnO composite developed by Nocera et al. (Kanan et al., 2009) and Xu et al. (Wang et al., 2012), respectively, were applied as catalysts to oxidize water into O_2. Co species are also effective catalysts for oxygen evolution from water because these compounds generate intermediate species with water oxidation active sites (Indra et al., 2013). $Co_3(PO_4)_2$ materials have been synthesized mainly by hydrothermal synthesis in the presence of a structure-directing agent, such as a template, and organophosphates to construct hybrid frameworks (Kumalah Robinson et al., 2011; Parlett et al., 2013). However, the preparation of hybrid $Co_3(PO_4)_2$ wherein nucleic acid ligands are used as scaffolds has not been fully investigated.

The present study describes the fabrication of hybrid PDGF-BB-targeted aptamer-inorganic $Co_3(PO_4)_2$ nanoflowers in a one-pot reaction (Scheme 1). The resulting nanoflowers were then used to achieve rapid detection of PDGF-BB. PDGF-BB-targeted aptamer ligands were used not only as the scaffold for $Co_3(PO_4)_2$ nanoflower formation but also to detect PDGF-BB with high sensitivity and selectivity. Therefore, multiple steps of the electrochemical biosensor fabrication could be achieved using single hybrid-aptamer nanoflowers as the sensitive layer. Simultaneously, BSA-templated $Co_3(PO_4)_2$ nanoflowers were prepared, immobilized with the PDGF-BB-targeted aptamer, and then used to detect PDGF-BB. The electrochemical approach was used to evaluate the efficiency of the developed aptasensors.

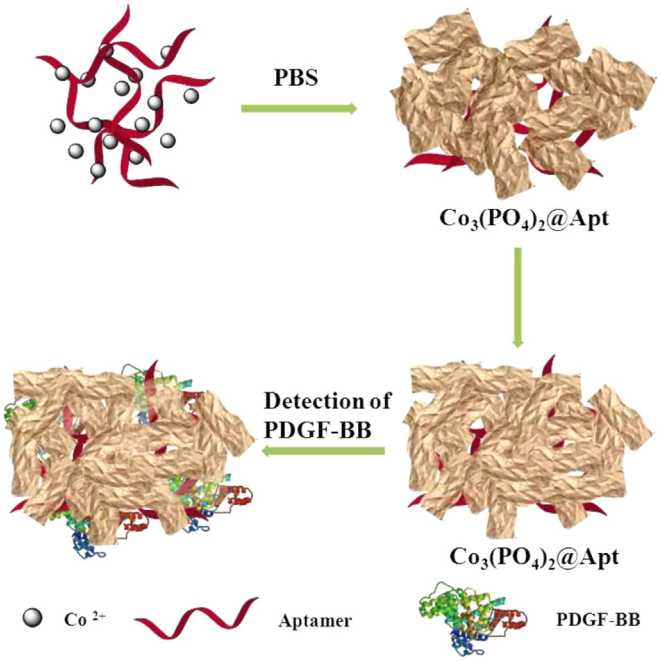

Scheme 1. Schematic diagram of the preparation of $Co_3(PO_4)_2$-based nanocomposites and their related electrochemical biosensor for detecting PDGF-BB.

2. Experiment

2.1. Materials

BSA with a molecular weight of 67000 was purchased from Shanghai Biolife Science and Technology Co., Ltd. (Shanghai, China). KH_2PO_4 and $Na_2HPO_4 \cdot 12H_2O$ were purchased from Sigma-Aldrich. $K_3[Fe(CN)_6]$ and $K_4[Fe(CN)_6] \cdot 3H_2O$ were supplied by Tianjin Fengchuan Reagent Co. Ltd. (Tianjin, China). Thrombin, lysozyme, PDGF-BB, PDGF-AA, PDGF-AB, and human immunoglobulin G (IgG) were obtained from Beijing SBS Genetech Co., Ltd. (Beijing, China). Other chemicals not mentioned here were used as received without further purification. Aqueous solutions were prepared with Milli-Q water obtained from a Millipore system ($\geq$ 18.2 MΩ cm).

Phosphate buffer solution (PBS) was prepared by mixing a stock standard solution of Na_2HPO_4 and NaH_2PO_4. Aptamer strands for detecting proteins were obtained from SBS Genetech Co., Ltd. (Beijing, China). The sequence of the PDGF-BB-targeted aptamer is 5'-CAG GCT ACG GCA CGT AGA GCA TCA CCA TGA TCC TG-3′.

2.2. Synthesis of $Co_3(PO_4)_2$-based nanocomposites

In a typical experiment, about 1.3 mL of aqueous $CoSO_4$ solution (120 mM) in molecular biology-grade water was added to 200 mL of PBS (pH 7.4) containing 20 mg of BSA, followed by incubation at 25 °C for 24 h. After incubation, the materials were separated by centrifugation, washed with distilled water, and dried in a vacuum oven at 60 °C for 24 h. For $Co_3(PO_4)_2$@Apt nanocomposite preparation, BSA was replaced by the PDGF-BB-targeted aptamer.

2.3. Construction of the fabricated aptasensors

A gold electrode (GE) with a diameter of 3 mm was polished with 1.0 and 0.3 μm alumina slurry, followed by ultrasonication in ultrapure water and ethanol. Subsequently, the electrode was electrochemically cleaned in 0.1 M H_2SO_4 by potential scanning between -0.2 and 1.6 V for 10 cycles. Finally, the electrode was rinsed thoroughly with water and dried under nitrogen gas.

To prepare the suspending agents, approximately 20 mg of $Co_3(PO_4)_2$-based nanocomposites were ultrasonically dispersed into 5 mL of deionized water. A 20 μL portion of the suspending agents was coated on the electrode and dried at 60 °C. The working electrode was fabricated by casting deionized water-impregnated $Co_3(PO_4)_2$@BSA or $Co_3(PO_4)_2$@Apt onto a GE.

2.4. Characterizations

Transmission electron microscopy (TEM) investigations were performed using a JEOL JSM-6490L V system. To observe the morphology of the samples, scanning electron microscopy (SEM) was performed on the JEOL JSM-6490LV. X-ray photoelectron spectroscopy (XPS) was performed on a VG ESCALAN HP photoelectron spectrometer equipped with an analyzer and preparation chambers with monochromatized Al-Kα X-ray radiation

(1486.6 eV). Fourier transform infrared (FTIR) spectra were recorded from samples in KBr pellets using a Nicolet 5700 FTIR instrument within the range of 400–4000 cm^{-1}. X-ray powder diffraction (XRD) was performed on a D8 advance (Bruker Corporation) operating at 50 mA and 30 kV using Cu Kα as a radiation source ($\lambda = 0.17890$ nm) and a 2θ range of 10–80°.

2.5. Electrochemical measurements

Cyclic voltammetry (CV) and electrochemical impedance spectroscopy (EIS) were performed using a CHI660E electrochemistry workstation (Chenhua CH Instrument Company, Shanghai, China) with a three-electrode system containing a platinum wire and bare or modified GE as the counter and working electrodes, respectively. All electrochemical experiments were carried out at room temperature (25 ± 1 °C). CV was performed stepwise in 20 mL of a 5 mM $K_3[Fe(CN)_6]/K_4[Fe(CN)_6]$ (1:1) mixture as a redox probe in PBS (containing 0.1 M KCl) at potentials ranging from −0.2 to 0.8 versus Ag/AgCl at a scan rate of 100 mV/s.

3. Results and discussion

3.1. Chemical components of $Co_3(PO_4)_2$-based nanocomposites

The chemical structure of the $Co_3(PO_4)_2$-based nanocomposites was characterized by FTIR (Fig. S1). Additionally, To evaluate the chemical components of the $Co_3(PO_4)_2$-based nanocomposites, XPS measurements were carried out. The XPS survey spectra of the $Co_3(PO_4)_2$@BSA and $Co_3(PO_4)_2$@Apt nanocomposites (Fig. S2); here, four strong signals of C 1s, O 1s, P 2p, and Co 2p and a weak signal of N 1s can be observed. The spectra demonstrate that C 1s, N 1s, and O 1s originate from the organic components, i.e., BSA or the aptamer, whereas Co 2p results from $Co_3(PO_4)_2$. P 2p could be attributed to both the biomolecules and inorganic phases. Table S1 summarizes the percentages (%) of each element. The atomic percentages of Co 2p in the $Co_3(PO_4)_2$@BSA and $Co_3(PO_4)_2$@Apt nanocomposites are around 13.13% and 11.36%, respectively. In the $Co_3(PO_4)_2$@BSA nanocomposites, a very low signal of S 2p with a (content, 0.59%) was observed (Fig. S3); this element is attributed to the presence of BSA. Fig. 1 shows the core-level XPS spectra of C 1s, N 1s, P 2p, and Co 2p. The C 1s core-level XPS spectra of both samples (Fig. 1a) revealed three identical peaks at ~284.6, ~285.7, and ~288.1 eV; these peaks are attributed to C–C/C–H, C–O, and N–C=O groups, respectively. In the C 1s core-level spectra of the $Co_3(PO_4)_2$@BSA nanocomposites, an additional peak at ~292.5 eV, which is due to the π–π* bonds of the protein molecules (Lavorgna et al., 2013), may be observed. In N 1s core-level spectra (Fig. 1b), two peaks at ~399.1 and ~400.1 eV, which may be assigned to C–N/N–H and N–C=O groups (Pisarek et al., 2013), respectively, were observed. According to the peak area of the functional groups, the density of N–C=O groups in the $Co_3(PO_4)_2$@BSA nanocomposites is higher than that in the $Co_3(PO_4)_2$@Apt nanocomposites. In the present study, the presence of C 1s and N 1s signals proves that the nanocomposite contains the organic component. Figs. 1c and 2d show the substantial Co 2p and P 2p signals of the two samples. Two main peaks positioned at the binding energy sites of 780 and 796.4 eV, corresponding to the Co $2p_{3/2}$ and Co $2p_{1/2}$ orbitals, respectively, may be observed. The Co $2p_{3/2}$ peak located at 778.1–778.3 eV corresponds to Co–Co bonding, and the peak located

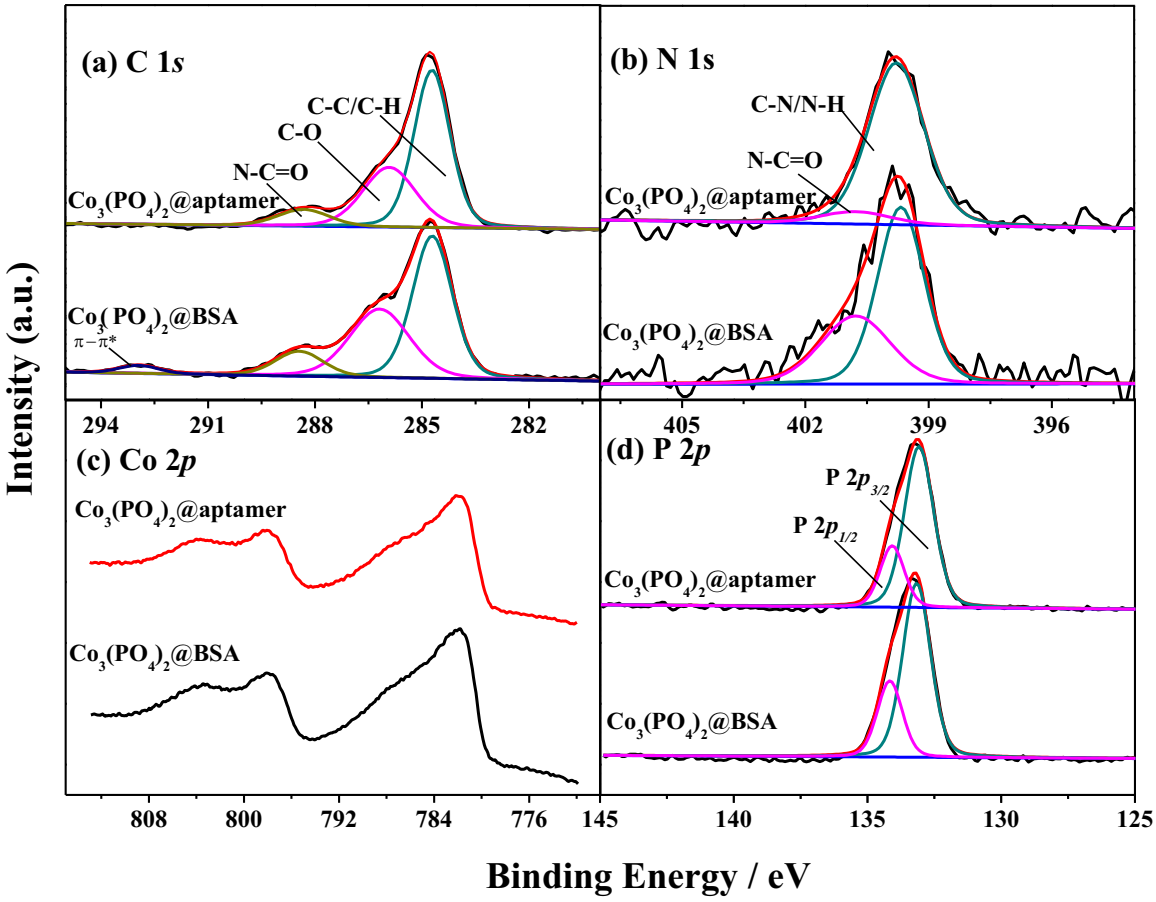

Fig. 1. (a) C 1s, (b) N 1s, (c) Co 2p and (d) P 2p core-level XPS spectra of $Co_3(PO_4)_2$@BSA and $Co_3(PO_4)_2$@Apt nanocomposites.

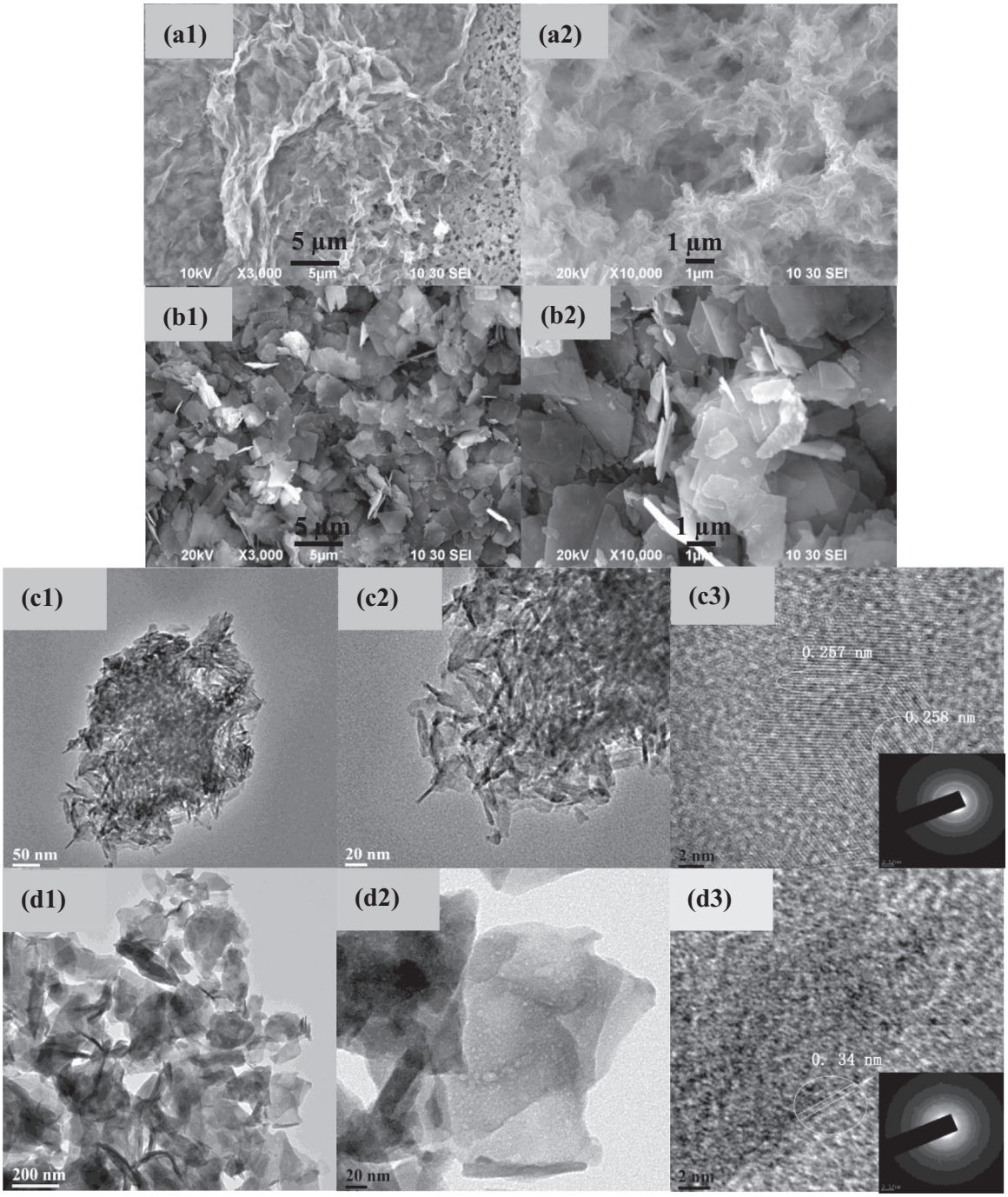

Fig. 2. SEM images of (a1–a2) $Co_3(PO_4)_2$@BSA and (b1–b2) $Co_3(PO_4)_2$@Apt nanocomposites and HR-TEM images of (c1–c3) $Co_3(PO_4)_2$@BSA and (d1–d3) $Co_3(PO_4)_2$@Apt nanocomposites (Inset of (c3) and (d3): SAED patterns of $Co_3(PO_4)_2$@BSA and $Co_3(PO_4)_2$@Apt nanocomposites, respectively.).

around 780 eV is due to Co-O bonding (Peng et al., 2005; Zhang et al., 2014). The P 2p core-level spectra of phosphate groups can be curve-fitted into two peaks with binding energies of 133.5 and 134.5 eV; these peaks are assigned as P $2p_{3/2}$ and P $2p_{1/2}$, respectively.

3.2. Surface morphology of $Co_3(PO_4)_2$-based nanocomposites

Typical SEM and TEM images of the as-synthesized $Co_3(PO_4)_2$-based nanocomposites are shown in Fig. 2. Clear differences between the $Co_3(PO_4)_2$@BSA and $Co_3(PO_4)_2$@Apt nanocomposites are observed. While agaric-like folded nanosheets in BSA-incorporated $Co_3(PO_4)_2$-based nanocomposites are evident (Fig. 2a1 and a2), the $Co_3(PO_4)_2$@Apt nanocomposite consists of large quantities of irregular nanoflake-like structures (Fig. 2b1 and b2). Bright-field TEM images of $Co_3(PO_4)_2$@BSA clearly show that the continuous nanosheets assemble into 3D agaric-like structures (Fig. 2c1–c3). HR-TEM examinations reveal that the as-synthesized nanoflakes are well crystallized. The inset in Fig. 2a3 shows the selected area electron diffraction (SAED) patterns of the nanosheets. The SAED pattern is composed of polycrystalline diffraction rings, indicating the nanocrystalline nature of the ligaments in the as-prepared folded nanosheets. Moreover, clear lattice spacings of about 0.258 and 0.34 nm between adjacent lattice planes correspond to the interplanar spacing of the (132) and (131) planes of the $Co_3(PO_4)_2$@BSA agaric-like folded nanosheets (JCPDS

No. 82-0303). Very weak characteristic peaks at 27.12° and 34.98° (curve *i* in Fig. S4), which may be attributed to the (131) and (132) planes, respectively, of the $Co_3(PO_4)_2$@BSA nanoflowers, are observed in the XRD spectrum of the products.

TEM images of the $Co_3(PO_4)_2$@Apt nanocomposite (Fig. 2d1–d3) demonstrate thin, transparent, and separated nanosheets overlaying each other. Ambiguous polycrystalline diffraction rings can also be observed in the SAED pattern of $Co_3(PO_4)_2$@Apt (inset of Fig. 2d3), thereby suggesting its low nanocrystalline or amorphous structural nature. This observation is confirmed by the absence of clear lattice spacings between adjacent lattice planes (Fig. 2d3). No substantial peak is observed in the XRD pattern of the $Co_3(PO_4)_2$@Apt nanostructures (curve *ii* in Fig. S4). All of these results indicate that the $Co_3(PO_4)_2$@Apt nanocomposite is amorphous because of the presence of large amounts of aptamer strands in the product.

3.3. Formation mechanism of $Co_3(PO_4)_2$@-based nanocomposites

We propose a three-step mechanism to describe the self-assembly of BSA-incorporated organic–inorganic hybrid nanoflowers (Fig. S5). At the early growth stage (Fig. S5a), primary agaric-like nanoflowers of $Co_3(PO_4)_2$ are formed. At this stage, protein molecules bind Co^{2+} ions through coordination bonds with the amide groups in the protein backbone. These complexes then provide a location for nucleation to initiate biomineralization of $Co_3(PO_4)_2$. Subsequently, the formed protein-Co^{2+} agaric-like nanoflowers combine into large agglomerates layer-by-layer (3–12 h, Step 2, Figs. S5b–S5d). The kinetically controlled growth of the $Co_3(PO_4)_2$ nanostructures results in a porous and 3D network, which helps adsorb much more biomolecules for further usage. Finally, the growth process of $Co_3(PO_4)_2$ nanoflowers continues until the complete formation of closed structures (24–72 h, Step 3, Figs. S5e and S5f) is achieved. Hence, $Co_3(PO_4)_2$ nanoflowers with loose and porous nanostructures prepared for 12 h were used in further experiments as scaffold materials to immobilize biomolecules for detection of target molecules.

For the $Co_3(PO_4)_2$@Apt nanocomposite, because of the lack of interaction between aptamer and $Co_3(PO_4)_2$, aptamer can not serve as a nucleation site for the formation of primary nanoparticles of $Co_3(PO_4)_2$ and further act as a capping agent that helps the particles maintain a agaric-like morphology. Thereby, large quantities of irregular nanoflake-like structures were observed in the $Co_3(PO_4)_2$@Apt nanocomposite.

3.4. Electrochemical characterization of the developed aptasensors fabrication steps

The electrochemical characteristics of the as-developed aptasensors based on $Co_3(PO_4)_2$@BSA and $Co_3(PO_4)_2$@Apt

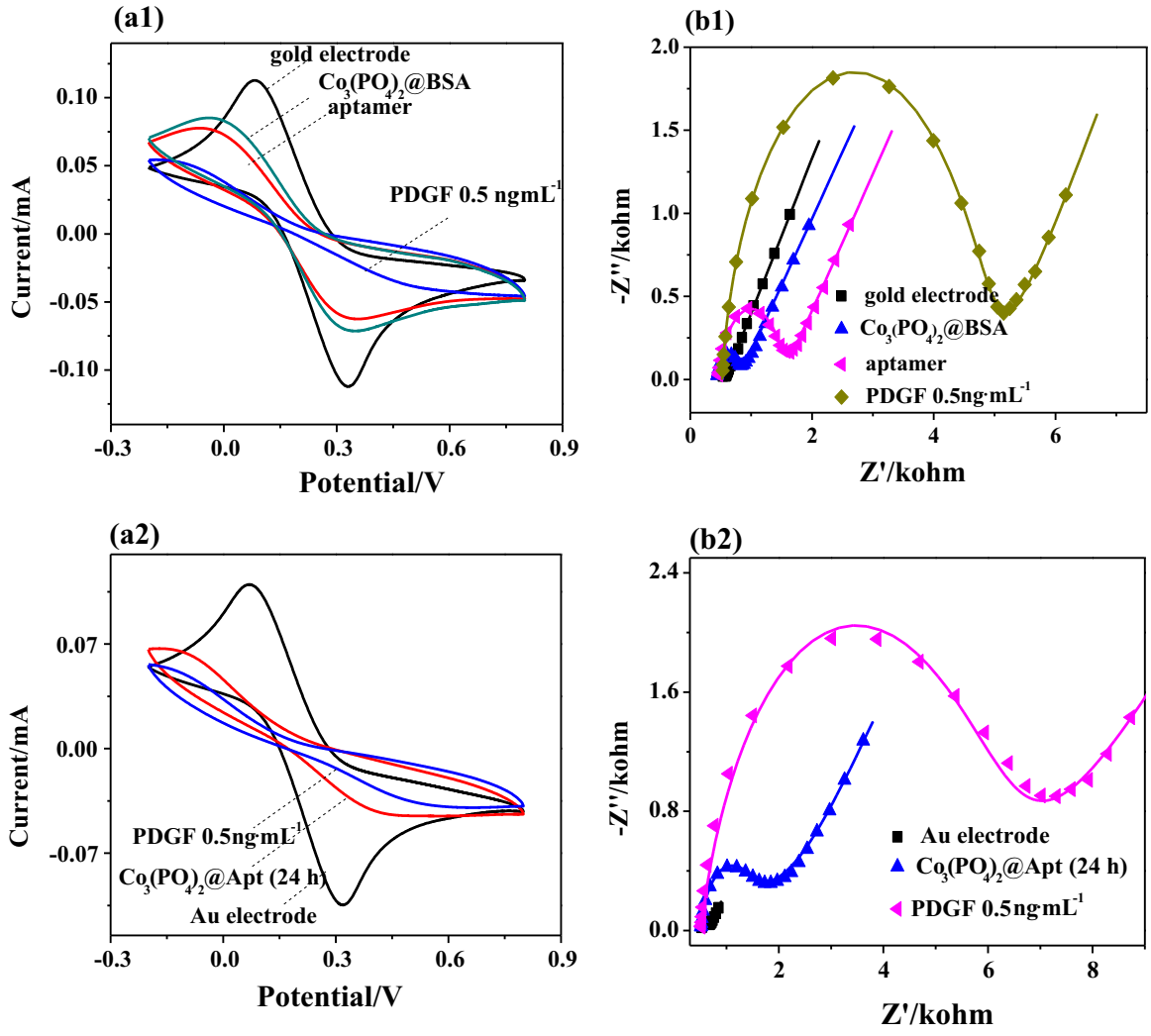

Fig. 3. (a1, b1) Cyclic voltammograms at a scan rate of 50 mV s^{-1} and (a2, b2) Nyquist plots of EIS recorded from 0.1 to 10^5 Hz in 10 mM $[Fe(CN)_6^{3-}]Fe(CN)_6^{4-}]$ (10 mM, 1:1) containing in 0.1 M KCl of $Co_3(PO_4)_2$@BSA- and $Co_3(PO_4)_2$@Apt-based electrochemical biosensor for detecting PDGF-BB, respectively.

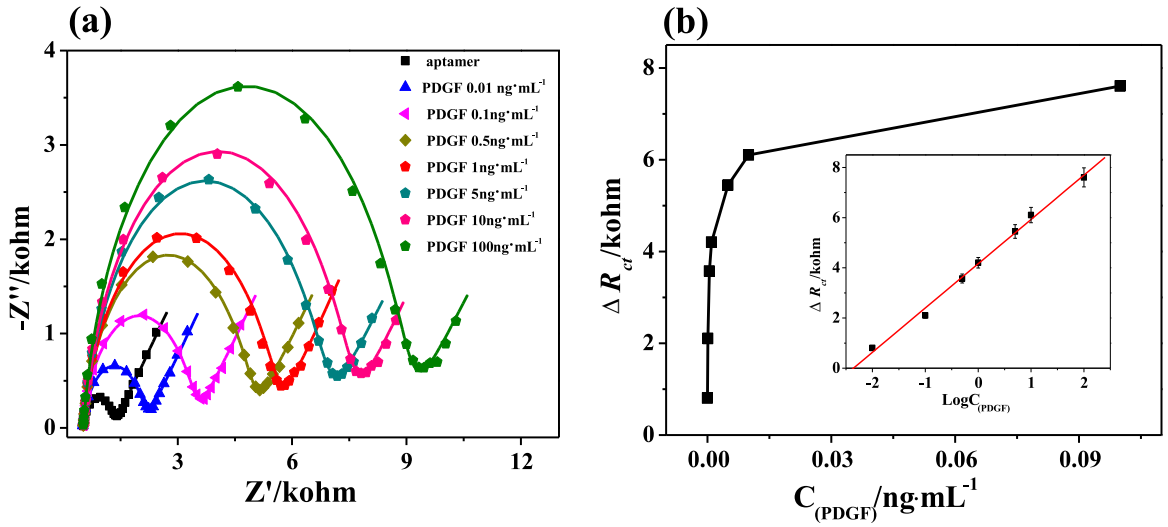

Fig. 4. (a) EIS response of the electrode modified with $Co_3(PO_4)_2$@BSA-Apt after recognition with different concentrations of PDGF-BB for 1 h and (b) calibration curve for change in electron-transfer resistance with logarithm of PDGF-BB.

nanocomposites were studied by CV and EIS. Fig. 3a1 shows the CVs of different modified electrodes in 1.0 mM $Fe(CN)_6^{3-/4-}$ solution containing 0.1 M KCl at a scan rate of 50 mV s^{-1}. The bare GE shows a well-defined redox peak corresponding to the reversible redox couple of $Fe(CN)_6^{3-/4-}$. After modification with $Co_3(PO_4)_2$@BSA on the GE, the redox peak current decreases significantly because the $Co_3(PO_4)_2$@BSA film presents a reduced effective electrochemical surface area, which can decrease electron transfer. When the aptamer is immobilized on the $Co_3(PO_4)_2$@BSA film, the redox peak currents are further reduced because the captured aptamer can severely hinder the electron transfer of $Fe(CN)_6^{3-/4-}$. The aptamer probe can prefold into a hair structure to achieve a sufficient interstitial space between immobilized aptamer sequences; this space facilitates the binding of the aptamer probe with the target molecules. Thus, when the PDGF molecules are adsorbed onto the composite electrode, the peak currents decrease.

EIS was performed in a 5 mM $K_3[Fe(CN)_6]/K_4[Fe(CN)_6]$ (1:1) mixture as a redox probe in PBS (containing 0.1 M KCl). Impedance spectra were collected at a potential of 0.21 V within the frequency range of 0.01 Hz to 100 kHz. EIS is generally used to characterize modified electrodes because it provides sensitive and immediate responses to changes in electroactive substances. In impedance spectra, the semicircle (in the high-frequency region) represents the electron transfer process, and the straight line (in the low-frequency region) corresponds to the diffusion process. Fig. 3a2 shows the detailed changes in the R_{ct} values during the aptasensor fabrication using $Fe(CN)_6^{3-/4-}$ as the electroactive redox probe. After modification with $Co_3(PO_4)_2$@BSA on the bare GE, the Nyquist plots display a standard EIS spectrum with an R_{ct} value of 0.36 kΩ, which is higher than that of the bare GE (0.0452 kΩ). This result indicates significant reduction of electrochemical signal due to the presence of the $Co_3(PO_4)_2$@BSA nanoflowers and a diffusion-limited electron transfer process. Findings also demonstrate that the nanoflowers can prevent electron transfer. As the aptamer is immobilized onto the composite electrode, it leads to a slight increase in the R_{ct} value (1.05 kΩ), thereby indicating that the negatively charged phosphate backbone hinders electron transfer. In the presence of PDGF-BB, the EIS spectrum exhibits a higher R_{ct} value with 4.73 kΩ. This observation may be attributed to the fact that target-aptamer binding events prevent the electroactive probe from reaching the electrode surface.

Fig. 3b1 and b2 shows the CV and EIS characterization results of the fabricated aptasensor based on $Co_3(PO_4)_2$@Apt nanocomposite. It exhibits a similar trend towards the PDGF-BB detection with the continuous decrease of the peak current in CVs during the procedure of the modification with $Co_3(PO_4)_2$@Apt nanocomposite and the determination of PDGF-BB (Fig. 3b1). During the EIS measurements (Fig. 3b2), the R_{ct} values increase from 0.153 kΩ in the bare GE to 0.623 kΩ in the $Co_3(PO_4)_2$@Apt-modified electrode, indicating repulsive interactions between the negatively charged phosphate groups of the aptamer in the $Co_3(PO_4)_2$@Apt nanocomposite and the $Fe(CN)_6^{3-/4-}$ probes. The R_{ct} values further increase to 4.5 kΩ after PDGF-BB is captured by the aptamer in the $Co_3(PO_4)_2$@Apt nanocomposite. During EIS, the efficiency of the added layer on the electrochemical properties of the modified electrode can be deduced from differences in R_{ct} ($\Delta R_{ct} = R_{ct,\ blank} - R_{ct}$) at each step. The ΔR_{ct} values of the $Co_3(PO_4)_2$@BSA- and $Co_3(PO_4)_2$@Apt-based aptasensors before and after PDGF-BB detection are 2.68 and 3.877 kΩ, respectively. Therefore, the detection efficiency of the $Co_3(PO_4)_2$@Apt-based aptasensor for PDGF-BB is higher than that of the $Co_3(PO_4)_2$@BSA-based electrochemical biosensor. As discussed above, large amounts of aptamer strands are incorporated into the 3D-network of the $Co_3(PO_4)_2$@Apt nanocomposite, thus facilitating the adsorption of PDGF-BB molecules. In the $Co_3(PO_4)_2$@BSA nanoflowers, the aptamer strands are first immobilized onto the nanocomposite surface. When the first layer of aptamer strands is anchored to the nanoflowers, repulsive interactions between the negatively charged phosphate groups of the aptamer molecules inhibit other oligonucleotides from adsorbing onto the nanocomposite (Zhang et al., 2012). Consequently, less amounts of aptamer strands can anchor onto the $Co_3(PO_4)_2$@BSA nanoflowers and fewer PDGF-BB molecules can be determined.

3.5. *Sensitivity, specificity, and stability of the developed aptasensors*

Quantitative monitoring of PDGF-BB was performed by impedance measurements using the constructed aptasensors based on $Co_3(PO_4)_2$@BSA and $Co_3(PO_4)_2$@Apt nanocomposites. The semicircle diameter in the Nyquist diagram for the immobilized $Co_3(PO_4)_2$@BSA-Apt nanoflowers electrode increases with increasing amount of PDGF-BB within the range of 0.01–100 ng mL^{-1} (Fig. 4**a**). The R_{ct} increase is defined as $\Delta R_{ct} = R_{PDGF\text{-}BB} - R_{apt}$, where $R_{PDGF\text{-}BB}$ is the R_{ct} value after PDGF-BB adsorption and R_{apt} is the impedance after aptamer immobilization onto the $Co_3(PO_4)_2$@BSA-modified GE. The linear equation is given as $\Delta R_{ct} = 4.09 + 1.65\ \log C_{PDGF\text{-}BB}$, and the detection limit (LOD) is

Table 1
Comparison of sensitivities from previous literature reports.

Electrode materials	Methods	Linear range	LOD	Refs.
Single-walled carbon nanotubes and multi-labeled graphene	Differential pulse voltammetry	0.31–108.5 μg mL^{-1}	0.248 μg mL^{-1}	(Bai et al., 2012)
Aptamer-protein nanowire	Chronocoulometry	3.1 ng mL^{-1} to 310 μg mL^{-1}	3.1 ng mL^{-1}	(Li et al., 2013)
Gold nanoparticles	Voltammograms	0.31–31 ng mL^{-1}	0.31 ng mL^{-1}	(Wang et al., 2009)
Aptamer-primed polymerase	Square wave voltammetry	50–500 ng mL^{-1}	18 pg mL^{-1}	(Huang et al., 2008)
Graphene oxide	Square wave voltammetry	0.01–100 ng mL^{-1}	5 pg mL^{-1}	(Qu et al., 2011)
Protein-templated cobaltous phosphate nanocomposites	EIS	0.01–100 ng mL^{-1}	3.7 pg mL^{-1}	This work

3.7 pg mL^{-1} (S/N=3) within the range of 0.01–100 ng mL^{-1} (Fig. 4b); here, the coefficient constant R^2 is 0.988. The developed aptasensors are also more sensitive than previously reported EIS sensors because of the large surface area of the 3D nanostructure, good biocompatibility, and high functionality of the $Co_3(PO_4)_2$-based nanomaterials and the high affinity between the aptamer and nanocomposite.

Limit detection of the fabricated aptasensor based on $Co_3(PO_4)_2$ @Apt nanocomposite was measured (Fig. S7). The Nyquist diagram gradually changes with increasing adsorbed concentration of PDGF-BB; this change is proportional to the logarithm of the PDGF-BB concentration. The linear relationship found is $\Delta R_{ct}=4.34+4.24\ \log C_{PDGF-BB}$ and the detection limit (LOD) is only as low as 61.5 pg mL^{-1} within the range of 0.5–100 ng mL^{-1} ($S/N=3$, $R^2=0.988$). Namely, the LOD determined for the $Co_3(PO_4)_2$ @Apt-based aptasensor is higher than that of the $Co_3(PO_4)_2$@BSA nanoflower-based sensor, which is unexceptedly. We conjecture that such a finding may be attributed to the possible bioactivity loss of the aptamer in the $Co_3(PO_4)_2$@Apt nanocomposite during nanocomposite preparation, thereby leading to relatively low affinity with PDGF-BB molecules. The two LODs obtained are still much lower than or comparable with those of previously reported aptasensors (Table 1).

To evaluate the specificity of $Co_3(PO_4)_2$@BSA-based aptasensor, EIS was performed to monitor the R_{ct} changes after incubating with different proteins, including BSA, IgG, lysozyme, thrombin, PDFG-AA, PDGF-AB and PDGF-BB, at the same concentration. No substantial change was detected after incubation of the developed aptasensor in BSA, IgG, lysozyme, thrombin, PDGF-AA and PDGF-AB, whereas PDGF-BB provides a significant R_{ct} change (Fig. S8). Therefore, the prepared aptasensor can distinguish between PDGF-BB and other proteins. The good specificity of the proposed electrochemical aptasensor is attributed to the specific binding between PDGF-BB and its targeted aptamer immobilized on $Co_3(PO_4)_2$@BSA. The stability of the aptasensor was determined after storage in a refrigerator at 4 °C for 15 d. After storage, the R_{ct} value only decreases by 5.6%. The developed aptasensor is therefore sufficiently stable for PDGF-BB detection. The intra-assay precision of the aptasensor was estimated by detecting PDGF-BB at two levels for five replicate determinations. At PDGF-BB concentrations of 0.5 and 10 ng mL^{-1}, the relative standard deviations (RSDs) of the intra-assay using the developed aptasensor based on $Co_3(PO_4)_2$@BSA are 3.8% and 4.6%, respectively, thereby indicating acceptable precision. The reproducibility of the aptasensor for PDGF-BB was evaluated through five replicate measurements of an analyte batch in the same solution; the RSD obtained is 4.9%. Thus, the fabricated aptasensor shows excellent reproducibility.

3.6. Real samples

To validate the applicability of the fabricated sensor further, PDGF-BB contents in human serum samples collected from three healthy people were determined. Approximately 0.1 mL of serum sample was added to 10 mL of PBS (0.1 M) and detected with the constructed aptasensors (Table S2). The diluted serum samples were obtained by adding different volumes of PBS. The different target concentrations obtained by the developed strategy are in good agreement with the added concentrations, and the relative deviations obtained are not more than 4.8%. Additionally, the different diluted real serum samples were determined by the fabricated biosensor and ELISA method, respectively. As showed in Table S3, the results of the serum samples test are acceptable, indicating that the concentration of PDGF-BB in healthy persons were 0.051 ng mL^{-1}, approximately (Wang et al., 2013; Zhang et al., 2015a). Therefore, application of the developed aptasensors for PDGF-BB detection in human serum samples is feasible.

4. Conclusions

In summary, a novel EIS electrochemical aptasensor for the sensitive PGDF-BB detection was developed using inorganic–organic nanomaterials as the sensing layer. $Co_3(PO_4)_2$-based nanocomposites were synthesized via a facile self-assembly approach assisted by biomolecules, including BSA and aptamer; these nanocomposites were applied to the modified electrode to achieve good electro-activated performance. 3D-nanostructured $Co_3(PO_4)_2$ @BSA and $Co_3(PO_4)_2$@Apt nanocomposites exhibited large surface active sites, good biocompatibility, and high functionality. The fabricated aptasensor based on $Co_3(PO_4)_2$@BSA could detect PDGF-BB concentrations as low as 3.7 pg mL^{-1} whereas the $Co_3(PO_4)_2$ @Apt biosensor could detect PDGF-BB concentrations only as low as 61.5 pg mL^{-1}. Differences observed are attributed to the loss of bioactivity of the aptamer in the $Co_3(PO_4)_2$@Apt nanocomposites. In this study, $Co_3(PO_4)_2$@Apt was used not only as an adsorption matrix but also as a protein affinity enhancer. Therefore, the $Co_3(PO_4)_2$@Apt-based aptasensor is a promising electrode nanomaterial that can generate high-performance EIS responses and significantly enhance the detection signal for the designed assay. Other applications of $Co_3(PO_4)_2$-based new nanomaterials should be explored in future work.

Acknowledgment

This work was supported by Program for the National Natural Science Foundation of China (NSFC: Account No. 51173172) and Innovative Technology Team of Henan Province (Account No. C20150023).

Appendix A. Supplementary material

Supplementary data associated with this article can be found in the online version at http://dx.doi.org/10.1016/j.bios.2015.12.095.

References

Bai, L., Yuan, R., Chai, Y., Zhuo, Y., Yuan, Y., Wang, Y., 2012. Biomaterials 33 (4), 1090–1096.

Buchdunger, E., Cioffi, C.L., Law, N., Stover, D., Ohno-Jones, S., Druker, B.J., Lydon, N. B., 2000. J. Pharmacol. Exp. Ther. 295 (1), 139–145.
Chang, C.C., Wei, S.C., Wu, T.H., Lee, C.H., Lin, C.W., 2013. Biosens. Bioelectron. 42 (15), 119–123.
Chen, S., Chen, Y., Zhang, X., Qian, H., Chen, W., Xie, W., 2008. Gene Ther. 15 (21), 1424–1435.
Cheng, W., Ding, S., Li, Q., Yu, T., Yin, Y., Ju, H., Ren, G., 2012. Biosens. Bioelectron. 36 (1), 12–17.
Das, B.K., Tlili, C., Badhulika, S., Cella, L.N., Chen, W., Mulchandani, A., 2011. Chem. Commun. 47 (13), 3793–3795.
Du, Y., Li, B., Wang, F., Dong, S., 2009. Biosens. Bioelectron. 24 (7), 1979–1983.
Fleming, T.P., Saxena, A., Clark, W.C., Robertson, J.T., Oldfield, E.H., Aaronson, S.A., Ali, I.U., 1992. Cancer Res. 52 (16), 4550–4553.
Ge, J., Lei, J., Zare, R.N., 2012. Nat. Nanotechnol. 7 (7), 428–432.
He, J.L., Yang, Y.F., Shen, G.L., Yu, R.Q., 2011. Biosens. Bioelectron. 26 (10), 4222–4226.
Hianik, T., Wang, J., 2009. Electroanal 21 (11), 1223–1235.
Huang, Y., Nie, X.M., Gan, S.L., Jiang, J.H., Shen, G.L., Yu, R.Q., 2008. Anal. Biochem. 382 (1), 16–22.
Huang, Y., Ran, X., Lin, Y., Ren, J., Qu, X., 2015. Chem. Commun. 51 (21), 4386–4389.
Indra, A., Menezes, P.W., Zaharieva, I., Baktash, E., Pfrommer, J., Schwarze, M., Dau, H., Driess, M., 2013. Angew. Chem. Int. Ed. 52 (50), 13206–13210.
Ishii, Y., Tajima, S., Kawarada, H., 2011. Appl. Phys. Express 4 (2), 027001.
Janeway, K.A., Liegl, B., Harlow, A., Le, C., Perez-Atayde, A., Kozakewich, H., Corless, C.L., Heinrich, M.C., Fletcher, J.A., 2007. Cancer Res. 67 (19), 9084–9088.
Kanan, M.W., Surendranath, Y., Nocera, D.G., 2009. Chem. Soc. Rev. 38 (1), 109–114.
Kumalah Robinson, S.A., Mempin, M.V.L., Cairns, A.J., Holman, K.T., 2011. J. Am. Chem. Soc. 133 (6), 1634–1637.
López-Gallego, F., Yate, L., 2015. Chem. Commun. 51 (42), 8753–8756.
Lau, C.K., Yang, Z.F., Ho, D.W., Ng, M.N., Yeoh, G.C., Poon, R.T., Fan, S.T., 2009. Clin. Cancer Res. 15 (10), 3462–3471.
Lavorgna, M., Romeo, V., Martone, A., Zarrelli, M., Giordano, M., Buonocore, G., Qu, M., Fei, G., Xia, H., 2013. Eur. Polym. J. 49 (2), 428–438.
Li, C., Wang, Z., Gao, T., Duan, A., Li, G., 2013. Chem. Commun. 49 (36), 3760–3762.
Lin, Z., Xiao, Y., Yin, Y., Hu, W., Liu, W., Yang, H., 2014. ACS Appl. Mater. Interf. 6 (13), 10775–10782.
Liu, X., Li, Y., Zheng, J., Zhang, J., Sheng, Q., 2010. Talanta 81 (4), 1619–1624.
Parlett, C.M., Wilson, K., Lee, A.F., 2013. Chem. Soc. Rev. 42 (9), 3876–3893.
Peng, Y., Liew, T., Song, W., An, C., Teo, K., Chong, T., 2005. J. Supercond. 18 (1), 97–103.
Pisarek, M., Roguska, A., Marcon, L., Andrzejczuk, M., Janik-Czachor, M., 2013. Arch. Met. Mater. 58 (1), 261–267.
Qu, F., Lu, H., Yang, M., Deng, C., 2011. Biosens. Bioelectron. 26 (12), 4810–4814.
Sun, J., Ge, J., Liu, W., Lan, M., Zhang, H., Wang, P., Wang, Y., Niu, Z., 2014. Nanoscale 6 (1), 255–262.
Wang, J., Meng, W., Zheng, X., Liu, S., Li, G., 2009. Biosens. Bioelectron. 24 (6), 1598–1602.
Wang, P., Song, Y., Zhao, Y., Fan, A., 2013. Talanta 103 (15), 392–397.
Wang, Y., Wang, Y., Jiang, R., Xu, R., 2012. Ind. Eng. Chem. Res. 51 (30), 9945–9951.
Yuan, Y., Yuan, R., Chai, Y., Zhuo, Y., Ye, X., Gan, X., Bai, L., 2012. Chem. Commun. 48 (38), 4621–4623.
Zayats, M., Huang, Y., Gill, R., Ma, C., Willner, I., 2006. J. Am. Chem. Soc. 128 (42), 13666–13667.
Zelada-Guillén, G.A., Bhosale, S.V., Riu, J., Rius, F.X., 2010. Anal. Chem. 82 (22), 9254–9260.
Zhang, J.J., Cao, J.T., Shi, G.F., Liu, Y.M., Chen, Y.H., Ren, S.W., 2015a. Talanta 141 (15), 158–163.
Zhang, N., Shi, J., Mao, S.S., Guo, L., 2014. Chem. Commun. 50 (16), 2002–2004.
Zhang, Z., Li, G., Yan, F., Zhang, Z., Fang, S., 2012. Chin. J. Chem. 30 (2), 259–266.
Zhang, Z., Zhang, Y., Song, R., Wang, M., Yan, F., He, L., Feng, X., Fang, S., Zhao, J., Zhang, H., 2015b. Sens. Actuators B – Chem. 211, 310–317.
Zhu, D., Yan, Y., Lei, P., Shen, B., Cheng, W., Ju, H., Ding, S., 2014. Anal. Chim. Acta 846 (10), 44–50.
Zhu, D., Zhou, X., Xing, D., 2010. Biosens. Bioelectron. 26 (1), 285–288.
Zuo, X., Song, S., Zhang, J., Pan, D., Wang, L., Fan, C., 2007. J. Am. Chem. Soc. 129 (5), 1042–1043.